Astronomical Notes
Astronomische Nachrichten

Secondary tearing mode in the nonlinear evolution of magnetorotational instability

T. Tatsuno and **W. Dorland**

Center for Scientific Computation and Mathematical Modeling, The University of Maryland, College Park 20742, Maryland, USA

Received 2008 May 15, accepted 2008 Jun 28
Published online 2008 Aug 30

Key words accretion disks – instabilities – magnetic fields – magnetohydrodynamics (MHD) – plasmas

Numerical investigation of the two-dimensional magnetic reconnection is given in the context of the nonlinear evolution of the Magneto-Rotational Instability (MRI). With a careful comparison to various theories using both one- and two-dimensional analysis, it is found that a new stabilizing effect of the centrifugal force on tearing instability must be present in the specific geometry of the MRI. Magnetic reconnection might play a key role to the formation of the nonaxisymmetric structures observed in MRI experiments. The results may also be useful for the estimate of the accretion rate in various astrophysical objects.

Astron. Nachr. / AN **329**, No. 7, 688 – 700 (2008) / **DOI** 10.1002/asna.200811013

WILEY-VCH

Astron. Nachr. / AN **329**, No. 7, 688 – 700 (2008) / **DOI** 10.1002/asna.200811013

Secondary tearing mode in the nonlinear evolution of magnetorotational instability

T. Tatsuno⋆ and **W. Dorland**

Center for Scientific Computation and Mathematical Modeling, The University of Maryland, College Park 20742, Maryland, USA

Received 2008 May 15, accepted 2008 Jun 28
Published online 2008 Aug 30

Key words accretion disks – instabilities – magnetic fields – magnetohydrodynamics (MHD) – plasmas

Numerical investigation of the two-dimensional magnetic reconnection is given in the context of the nonlinear evolution of the Magneto-Rotational Instability (MRI). With a careful comparison to various theories using both one- and two-dimensional analysis, it is found that a new stabilizing effect of the centrifugal force on tearing instability must be present in the specific geometry of the MRI. Magnetic reconnection might play a key role to the formation of the nonaxisymmetric structures observed in MRI experiments. The results may also be useful for the estimate of the accretion rate in various astrophysical objects.

1 Introduction

Magnetic reconnection is one of the most fundamental phenomena in plasmas. It often entails vastly multiscale physics, brings about the change of global topology, converts magnetic energy into particle energy such as heat and acceleration and plays a very important role in the turbulent dynamo phenomena. While a fairly deep study and understanding have been made for the idealized steady reconnecting system by taking various physical effects into account, the understanding of reconnection in the complex development of the nonlinear plasma phenomena has not been achieved even with a simplest model. Here we try to investigate such a problem, namely the dynamic magnetic reconnection in the nonlinear evolution of the background plasma using the simplest model, two-dimensional incompressible magnetohydrodynamics (MHD). We explore the validity of several idealized theories on a dynamical system, and report that the problem is not so straightforward as one might expect. This is the first step to the understanding of the dynamic magnetic reconnection in the real physical system (developing system rather than an idealized stationary system).

In this paper we focus on the nonlinear development of the Magnetorotational instability (MRI) for our reconnection study. The first calculation of the MRI goes back to Velikhov (1959) and Chandrasekhar (1960), but it is after Balbus & Hawley (1991) that it has attracted attention for explaining accretion flows in various astrophysical objects. It has not been widely discussed so far, but in order for both the accreting matter and the angular-momentum-transporting matter to be detached from the main body of the magnetized plasma, magnetic reconnection has to take place in the nonlinear evolution of the MRI (Hawley & Balbus 1991; Machida & Matsumoto 2003). In this sense magnetic reconnection should be somehow related to, or might even govern the actual accretion rate. Dynamic magnetic reconnection is analyzed in other contexts such as supernova shock (Tanuma et al. 2001), Parker instability (Tanuma et al. 2003) and turbulent MHD plasmas (Lazarian & Vishniac 1999), however, there is no dedicated analysis in the nonlinear evolution of MRI.

Recently there are several experimental efforts being made to clarify the physics of the MRI (Sisan et al. 2004; Ji et al. 2006; Stefani et al. 2006; Stefani et al. 2007; Wang et al. 2007).

In the spherical experiment at Maryland using liquid sodium (Sisan et al. 2004), coupled velocity and magnetic field fluctuations are observed above critical applied magnetic field. These fluctuations mostly show nonaxisymmetric structures while the primary MRI mode is expected axisymmetric. Nevertheless the threshold of the applied magnetic field seems to agree quite well with the theoretical predictions of the stability boundary (Tillotson 2007). Cylindrical experiments are also being carried out using liquid metal (Ji et al. 2006; Stefani et al. 2006; Stefani et al. 2007) and plasma (Wang et al. 2007). PROMISE device (Stefani et al. 2006) makes an experiment with a helical field using liquid metal alloy. For a fixed azimuthal field strength they have increased the axial field and observed increased level of axial velocity fluctuations in agreement with numerical predictions. They also observed nonaxisymmetric fluctuation in some parameter regimes (Stefani et al. 2007). These nonaxisymmetric structure may be attributed to the secondary instability of some sort, one of such an example is the fluid dynamical wavy mode (Davey, Diprima &

⋆ Corresponding author: tatsuno@umd.edu

Stuart 1968). However, as the critical Reynolds number of the wavy instability seems to increase in the presence of the magnetic field (Tabeling 1981; Willis & Barenghi 2002), one might speculate that other MHD instabilities, such as tearing mode, the three-dimensional version of the reconnection presented here, might create the nonaxisymmetric fluctuation. Thus, it is very important to understand the dynamics of the magnetic reconnection in this sense as well.

In this paper we investigate various (linear) properties of the two-dimensional (2D) magnetic reconnection occurring in the context of the laboratory MRI experiment. We first show the normalized 2D equations for MRI in Sect. 2. Using our upgraded reduced MHD code (Tatsuno & Dorland 2006), we show when and how reconnection event takes place in Sect. 3 including the general nonlinear evolution of the MRI. Section 4 is the main part of the paper. We investigate the validity of various linear reconnection theory (tearing mode) using one-dimensional (1D) approximation (Furth, Killeen & Rosenbluth 1963; Coppi et al. 1976; Paris 1982) and also make the 2D linearized simulation for the comparison with other 2D results (Nishikawa & Sakai 1982; Paris 1987). We observe a beautiful 2D tearing eigenfunction during reconnection, and conclude that reconnection is attributed to the tearing instability of the opposing radial magnetic field which is created by the nonlinear evolution of the MRI. Note, however, that the creation of the magnetic null (X-point) is not necessarily attributed to the tearing mode. In some parameter regimes, X-point is created passively by the MRI but reconnection does not continue unless the surrounding geometry is made tearing unstable. For sufficiently high magnetic Reynolds number we observed a creation of the secondary island, which is briefly summarized in Sect. 5 with a comparison to the tearing instability of the current sheet (Bulanov, Sakai & Syrovatskii 1979). Finally, our conclusion is given in Sect. 6.

2 Reduced MHD equations for MRI

2.1 Formulation

We employ the 2D incompressible MHD equations in the r-z plane of the cylindrical configuration (r, θ, z). Let

$$\boldsymbol{v} = \nabla \times [\phi(r,z)\nabla\theta] + r v_\theta(r,z)\nabla\theta, \tag{1}$$

$$\boldsymbol{B} = \nabla \times [\psi(r,z)\nabla\theta] + r B_\theta(r,z)\nabla\theta, \tag{2}$$

and define

$$\omega = -(\nabla\times\boldsymbol{v})_\theta = \partial_r\left(\frac{1}{r}\partial_r\phi\right) + \frac{1}{r}\partial_z^2\phi =: \nabla_*^2\phi, \tag{3}$$

$$j = -(\nabla\times\boldsymbol{B})_\theta = \partial_r\left(\frac{1}{r}\partial_r\psi\right) + \frac{1}{r}\partial_z^2\psi = \nabla_*^2\psi, \tag{4}$$

$$[f,g] = \partial_r f\partial_z g - \partial_z f\partial_r f, \tag{5}$$

then the normalized 2D MHD equations for the incompressible plasmas yield

$$\partial_t\omega + \left[\phi, \frac{\omega}{r}\right] + \partial_z\left(\frac{v_\theta^2}{r}\right) = \left[\psi, \frac{j}{r}\right] + \partial_z\left(\frac{B_\theta^2}{r}\right) + \nu\nabla_*^2(r\omega), \tag{6}$$

$$\partial_t v_\theta + \frac{1}{r^2}[\phi, r v_\theta] = \frac{1}{r^2}[\psi, r B_\theta] + \nu\nabla_*^2(r v_\theta), \tag{7}$$

$$\partial_t\psi + \frac{1}{r}[\phi,\psi] = \eta r j, \tag{8}$$

$$\partial_t B_\theta + \left[\phi, \frac{B_\theta}{r}\right] - \left[\psi, \frac{v_\theta}{r}\right] = \eta\nabla_*^2(r B_\theta). \tag{9}$$

2.2 Boundary conditions

We consider a concentric cylinder with rigid ideal conducting walls at radii $r = r_{\rm in}$ and $r_{\rm out}$. We assume periodicity in the z direction.

2.2.1 Flow

Noslip boundary condition is imposed on the velocity field:

$$v_\theta(r_{\rm in}) = v_{\rm in} \quad \text{and} \quad v_\theta(r_{\rm out}) = v_{\rm out}. \tag{10}$$

Corresponding to

$$v_r = v_z = 0 \quad \text{at both walls}, \tag{11}$$

we may impose

$$\phi_{00} = 0, \quad \partial_r\phi_0|_{r_{\rm out}} = 0 \tag{12}$$

$$\partial_r(r\omega_0) = 0 \quad \text{at both walls} \tag{13}$$

for $k_z = 0$ component, and homogeneous Dirichlet condition for ϕ and the converted ω condition as is used in the slab case for $k_z \neq 0$ (Tatsuno & Dorland 2006).

2.2.2 Magnetic field

Ideally conducting wall yields

$$\boldsymbol{n}\cdot\boldsymbol{B} = 0, \quad \boldsymbol{n}\times\boldsymbol{j} = \boldsymbol{0} \quad \text{at both walls}, \tag{14}$$

which correspond to

$$\psi = \text{const} \qquad \text{in time and along walls}, \tag{15}$$

$$\partial_r(r B_\theta) = 0 \qquad \text{at both walls}, \tag{16}$$

where $\boldsymbol{n}$ represents a unit vector normal to the surface. Note that $\partial_t\psi = 0$ at wall would yield $\nabla_*^2\psi = 0$ from induction equation, together with $v_r = B_r = 0$.

In the vector form and for $k_z = 0$ component, $\partial_r B_z = 0$ is derived from $j_\theta = 0$ condition.

2.3 Description of the code

We have extended the slab code used in Tatsuno & Dorland (2006) to solve the cylindrical problem. This is a pseudo-spectral code with Chebyshev-Fourier expansion and solves reduced MHD Eqs. (6)–(9). Spectral accuracy is very useful for detailed diagnostics presented here. Normally the reconnection point does not lie exactly on top of the grid and one has to interpolate various physical quantities. Such interpolations are easily made with high accuracy by a spectral

scheme, which makes possible the sophisticated measurement of some complicated quantities. For the time integration it uses 3rd order Adams-Bashforth scheme for nonlinear terms and Crank-Nicholson scheme for linear terms.

The automatic resolution adjuster is implemented in the code, which uses an empirical error estimate at each time step and changes resolution globally by tapping zeroes in the Chebyshev (or Fourier) space or just removing small amplitudes. Time step is also automatically adjusted by the Courant condition.

Details of the upgrade we have made for the cylindrical version is described in Appendix A.

3 General evolution of MRI

In this section we show the general evolution of the MRI and show when and where magnetic reconnection takes place. We also discuss if saturation mechanism is attributed to it (Goodman & Xu 1994). Parameters are:

$$r_{\rm in} = 0.5, \quad r_{\rm out} = 1.5, \quad L_z = 1,$$
$$\nu = \eta = 1.5 \times 10^{-4}, \quad B_z = 0.15, \quad v_\theta(r_{\rm in}) = 1, \qquad (17)$$

which correspond to

$$R_{\rm m} = 10^4, \quad S = 1500, \quad P_{\rm m} = 1, \qquad (18)$$

where these dimensionless numbers are defined by

$$R_{\rm m} = \frac{V_{\theta,{\rm in}} r_{\rm out}}{\eta}, \quad S = \frac{B_z r_{\rm out}}{\eta}, \quad P_{\rm m} = \frac{\nu}{\eta}. \qquad (19)$$

Remember that we use velocity unit for B_z in our normalized equation.

We used the Keplerian flow profile ($v_\theta \sim r^{-1/2}$). Keplerian flow is not a stationary solution of the reduced MHD equations with finite dissipation rates, however, we do not care about the decay of the background flow since the time scale of the dissipation for a global structure is much slower than the dynamics we are interested in. In all of our simulations we use a magnetic Prandtl number of unity.

3.1 Linear growth

In order to prove the validity of our code, we show in Fig. 1 the growth rates taken from our 2D simulation as well as the results from an independent ideal ($\nu = \eta = 0$) shooting code. For this simulation we took $L_z = 2$ to have four unstable modes in the domain to compare with the shooting result. All four eigenvalues are sufficiently close but lower than the ideal ones. We also confirmed that the ideal run using our code gives exact growth rates on top of the line from the shooting code.

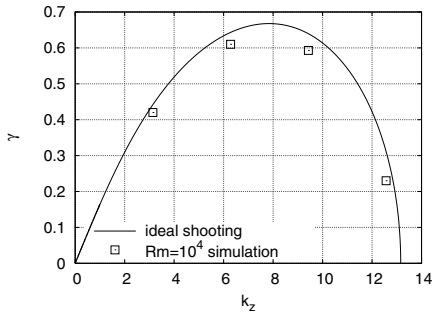

Fig. 1 Growth rates taken from ideal shooting code and from dissipative simulation.

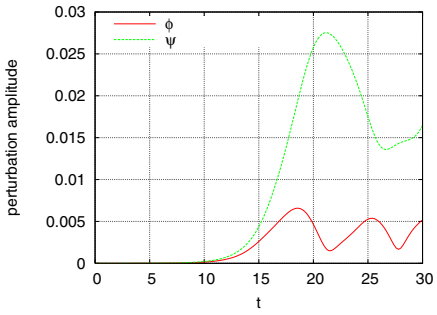

Fig. 2 (online colour at: www.an-journal.org) Time evolution of MRI perturbation amplitude.

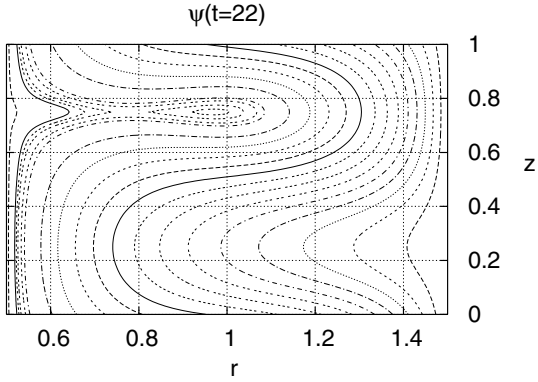

Fig. 3 Magnetic island is observed as a consequence of the reconnection. Contour scale is not equally spaced in order to highlight the island.

3.2 Saturation mechanism

Time evolution of the L^2 norm $||\phi - \phi_{\rm b}||$ and $||\psi - \psi_{\rm b}||$ are shown in Fig. 2, where the subscript b denotes the background field (axial field and azimuthal rotation). Saturation is first observed in ϕ about $t \simeq 18$ and that of ψ follows about $t \simeq 21$. As a consequence of the magnetic reconnection, magnetic island is observed at $t = 22$ as seen in Fig. 3. Notice the island around $(r, z) \simeq (0.95, 0.75)$. It is true that the coincidence of the peaking time of ψ curve and the appearance of the island implies some relationships, since stabilizing effect of the outflow stops at this stage, however, they are not simultaneous in all cases. As we show later,

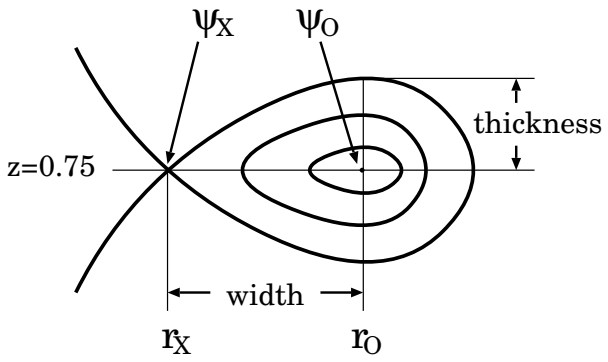

Fig. 4 Schematic view of the geometry of the magnetic island.

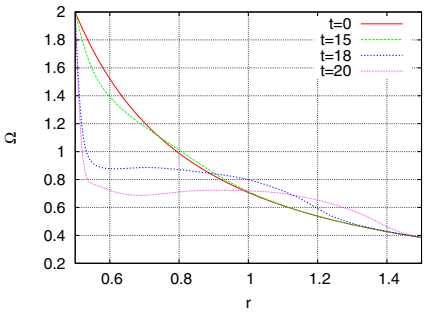

Fig. 5 (online colour at: www.an-journal.org) Radial profile of the averaged angular velocity.

there are cases where island appears long before the saturation of ψ or even before the peak of ϕ.

Why is only the outgoing field line stretched here while both incoming and outgoing fields are observed symmetric in the shearing slab simulation (Hawley & Balbus 1991)? It is surely related to the shape of the Taylor vortex which is narrower in the outgoing direction than the other. In fact the radial velocity at $(r, z) \simeq (0.95, 0.75)$ and $t = 18$ is about $v_r = 0.087$, which roughly agrees with the extension speed of the field line. Keeping in mind that the local MRI growth rate is proportional to the local rotation rate (Balbus & Hawley 1991), the MRI grows faster in the inside region due to its fast time scale, and the inward jet is killed by the inner boundary there.

If this is the case, there may be observed two or more outgoing jets simultaneously when higher wave number is more unstable. In fact we observed two (or three) fingers by extending the axial length twice, but as is observed by Hawley & Balbus (1992) and Liu, Goodman & Ji (2006), they eventually merge to form a single finger at a later time. Such phenomena are of great interest from the viewpoint of the magnetic reconnection since merging of fingers involve numbers of reconnection events. However, we concentrate on a formation of a single finger in this paper for the simplicity of the analysis, since the axial motion of the finger introduces the complex motion of the X-points. In our configuration with a single finger, the X-point moves only along the radial direction and not along the z-axis, which enables us the detailed diagnostics with a relatively simple implementation.

Figure 4 shows the schematic view of the geometry of the magnetic island. We implemented measurements of the flux functions at the X- ($\psi_{\rm X}$) and O-points ($\psi_{\rm O}$) and the island size as depicted. The inspection of the X- and O-points are made by detecting the sign change of B_z along the $z = 0.75$ line at every 0.01 time unit. From the time evolution of the magnetic island we confirmed that the island does not move in the z direction. It should be emphasized that we obtain $r_{\rm X}$ and $\psi_{\rm X}$ with a spectrally interpolated accuracy, which may not have been achieved by the finite difference scheme. In the present simulation the island is first observed at $t = 20.45$, grows until $t \simeq 24$ and eventually disappears at $t = 32.76$. Another island appears at $t = 37.24$ and follows more or less the same processes. Since our interest is on the dynamical evolution of the island, we do not ask the existence of the magnetic island in the final stationary state. Such a steady state itself may or may not exist, which may be separately an interesting subject of research and may be analyzed by tracing a steady state solution for various plasma parameters finding a bifurcation diagram (Rincon, Ogilvie & Proctor 2007).

From the fact that the saturation of ψ follows that of ϕ and that the magnetic reconnection starts at the saturated level of ψ, we conclude that the magnetic reconnection is not attributed to the saturation of the MRI as Goodman & Xu (1994) has proposed in the shearing sheet geometry. In our geometry, the created radial magnetic field strength is comparable to the original axial field while Goodman & Xu assumes $B_r \gg B_z$. Instead the saturation may be attributed to the disappearance of the drive as seen in the flat profile of the averaged angular velocity (See Fig. 5).

3.3 Profiles of various fields

Right before the emergence of the magnetic island, at $t = 20$, the profiles of various field quantities sliced along $r \simeq 0.8$ are shown in Fig. 6. There is a sharp counter-oriented radial magnetic field (B_r) centered at $z = 0.75$, which introduces the following magnetic reconnection event. The axial field (B_z) is almost zero around $z \simeq 0.75$. The azimuthal field (B_θ) also contains the counter-oriented component centered at the same place, which forms another source of the reconnection for a nonaxisymmetric perturbation. The radial velocity (v_r) shows a weak outflow representing a jet, and the profile of axial velocity (v_z) shows a weak counter-flow which may correspond to the inflow of the reconnection.

It is noted that Kelvin-Helmholtz instability does not occur for this configuration. This is because the magnitude of v_r and v_z are much smaller than the corresponding magnetic field components, and the spatial scale of v_θ is much larger than that of the other fields.

Now that we have finished explaining the environment of the reconnection event, so in the following sections we

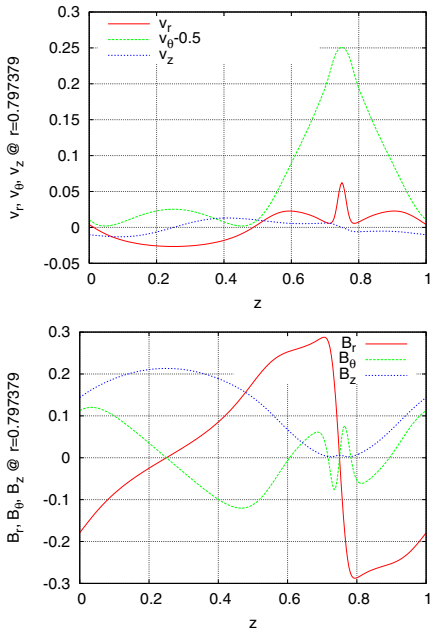

Fig. 6 (online colour at: www.an-journal.org) Various field profiles sliced along $r \simeq 0.8$ at $t = 20$.

proceed to actually characterize them in as much detail as possible.

4 First reconnection

4.1 Slab tearing model

The first thing we can come out of is the calculation of Δ' and the consequent growth rate in comparison to the basic tearing mode analysis (Furth et al. 1963; Coppi et al. 1976; Paris 1982). It actually turns out from the more detailed analysis that slab approximation is a too much simplification, but we here describe what we get from slab analysis for the comparison to the later sections.

4.1.1 Theory

Here we take the equilibrium

$$\boldsymbol{B}_0 = [B_x(z), B_y(z), 0], \tag{20}$$

which of course satisfies $\nabla \cdot \boldsymbol{B}_0 = 0$, and neglect all background velocity. Invoking slab geometry we also assume that curvature effect is negligible. We want to obtain Δ', the jump of the logarithmic derivative of the perturbed flux function in the outer region. The ordinary differential equation for the outer region where inertial effect may be neglected comes from the static vorticity equation

$$\nabla \times (\boldsymbol{B} \cdot \nabla \boldsymbol{B}) = 0. \tag{21}$$

Decomposing $\boldsymbol{B} = \boldsymbol{B}_0 + \boldsymbol{b}$, linearizing and assuming $\exp(\mathrm{i}k_x x)$ dependence yields

$$\frac{\mathrm{d}^2 b_z}{\mathrm{d}z^2} - \left(k_x^2 + \frac{F''}{F}\right) b_z = 0, \tag{22}$$

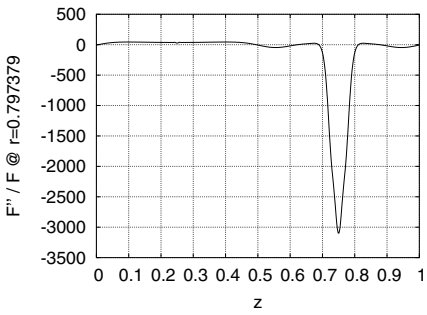

Fig. 7 Potential F''/F of the outer region ODE (22).

where we defined $F = k_x B_x$ (Biskamp 2000, [4.21]). By numerically solving (22), we estimate the jump of the logarithmic derivative

$$\Delta' = \frac{b_z'(+) - b_z'(-)}{b_z(z_{\mathrm{sheet}})}, \tag{23}$$

where z_{sheet} is the field reversal plane.

The growth rate may be obtained from (4.66) of Biskamp (2000) (see also Paris 1982):

$$-\frac{8}{\pi}\frac{\Delta'}{k_x}\left(\frac{\tau_{\mathrm{A}}}{\tau_\eta}\right)^{1/3} = \frac{\lambda^{5/6}\Gamma\left[(\lambda-1)/4\right]}{\Gamma\left[(\lambda+5)/4\right]}, \tag{24}$$

where

$$\lambda = \hat{\gamma}^{3/2} = \gamma^{3/2}\tau_\eta^{1/2}\tau_{\mathrm{A}}, \tag{25}$$

$$\tau_\eta = \frac{1}{k_x^2 \eta}, \tag{26}$$

$$\tau_{\mathrm{A}} = \frac{k_x}{F'}, \tag{27}$$

and Γ is the Gamma function. In the case of small Δ' we may take the small λ limit and recover the FKR result (Furth et al. 1963)

$$\gamma \simeq \left(\frac{2\Gamma(5/4)}{\pi\Gamma(3/4)}\right)^{4/5} \tau_{\mathrm{A}}^{-2/5}\tau_\eta^{-3/5}\left(\frac{\Delta'}{k_x}\right)^{4/5}. \tag{28}$$

The large Δ' limit may correspond to the limit $\lambda \to 1 - 0$ yielding

$$\gamma \simeq \tau_\eta^{-1/3}\tau_{\mathrm{A}}^{-2/3}, \tag{29}$$

which we call CGPR limit (Coppi et al. 1976).

4.1.2 Numerical estimate of Δ'

In order to invoke the discussion of the previous subsection, the boundary condition (BC) has to be determined. Let us find out what can be imposed at where. Since B_r looks like hyperbolic tangent profile around $z \simeq 0.75$ and B_r'' changes sign just below $z = 0.7$, we may spot the light on this point.

The function F''/F is shown in Fig. 7 at $t = 20$ and $r \simeq 0.8$. Notice that F''/F doesn't depend on the exact value of k_x. The minimum of the well is at $z = 0.75$ which

corresponds to the field reversal plane. There is a very mild concavity extending $0.1 \lesssim z \lesssim 0.4$, but this should not give a major effect and hence we neglect it in the following global calculation.

Since (22) takes exactly the form of the Schrödinger equation, we may regard F''/F as a potential and $-k_x^2$ as an energy. If the energy $-k_x^2$ is larger than the minimum of the potential well F''/F, there is a chance that we may have oscillatory solution, while smaller, we may not. This oscillatory behavior is needed for positive Δ' since otherwise two exponentially growing solutions from outside of the well would never match at the center of the well with positive Δ'.

Since the potential is bounded there is clearly a continuum above its maximum if we allow $-k_x^2$ to be positive. This fact brings a difficulty in the numerical estimate of the Δ' for small wave number. For example, the energy corresponding to $k_x = 0.5$ is too large ($-k_x^2 = -0.25$) and the solution is strongly affected by the existence of the continuum.

Exponential BC So we should consider lower energy and then we may impose the exponential BC at anywhere we want (we denote it $z_{\rm start}$) as far as it is outside of the well since the solution out of the well is going to be almost exponentially decaying. The gradient of b_z is given so that it matches the exponent corresponding to the local value of $\sqrt{k_x^2 + F''/F}$. For example, the exponential BC given at $z_{\rm start} = 0.6$ would be sufficient for $-k_x^2 \lesssim -100$ (The second smallest minima are around -50). Figure 8 shows the dependence of Δ' as a function of $z_{\rm start}$ for $k_x = 25$ with the exponential BC and the eigenfunction corresponding to $z_{\rm start} = 0.6$. For this setup, we conclude that $\Delta' \simeq 92$.

Periodic BC Another fact we may use for the BC is the periodicity of the system along z. Since the local minimum of the potential is about 40 around $z \simeq 0.25$, we simply conjecture that resistive layer is not formed for sufficiently negative $-k_x^2$. Then, from the symmetry around the current sheet at $z_{\rm sheet} = 0.75$, we may just flip the sign of b_z' there and continue integration to the right. Periodicity brings the solution to $z = 0$ when it crosses 1, we may integrate normally through $z = 0.25$ and match the solution with itself at the starting point $z_{\rm start} = 0.6$.

The scheme seems well-defined even for a fairly small k_x, and the resulting solution is shown in Fig. 9 for $k_x = 2$ and $k_x = 30$. The logarithmic plot is shown for $k_x = 30$, which represents a very good exponential behavior between the two field reversal planes. We also show the Δ' obtained from this scheme with a comparison to the previous exponential assumption. The scheme doesn't work with too high k_x since the exponential behavior becomes very rapid and we cannot match it even with a double precision computation. On the other hand, it does work for even smaller values of k_x than the exponential BC. So these two schemes are complementary, and the difference is negligible in the overlapping region as shown in Fig. 10. The critical wave number is obtained from the exponential BC and is about $k_x \simeq 40.8$.

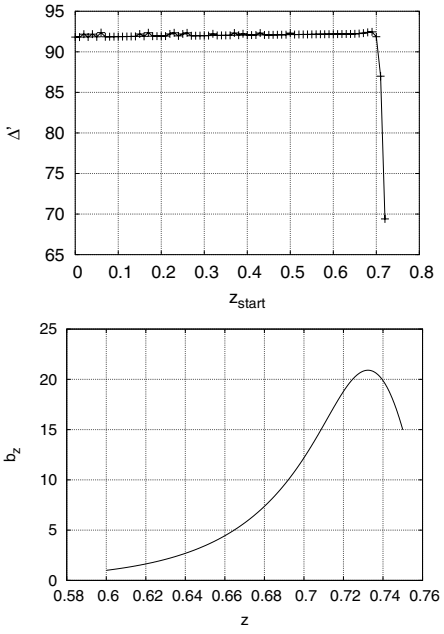

Fig. 8 Values of Δ' for various $z_{\rm start}$ and the eigenfunction corresponding to $z_{\rm start} = 0.6$.

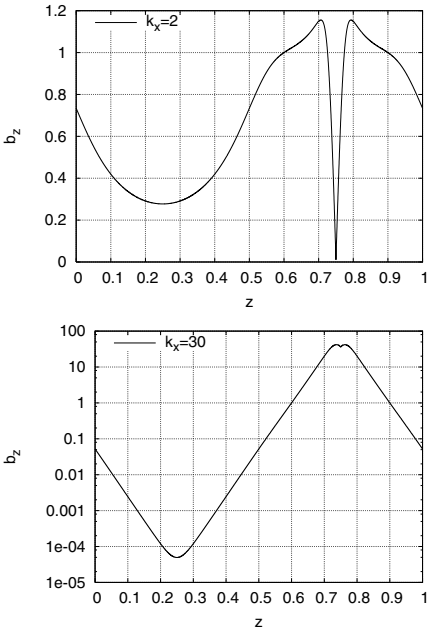

Fig. 9 Eigenfunction obtained with the periodic boundary condition.

4.1.3 Results

Now the question is how we use this result. We should of course have that $2\pi/k_{\rm max} < L_r$ where $k_{\rm max}$ and L_r denote the critical wave number for positive Δ' and the radial length of the stretched field line. But probably more strin-

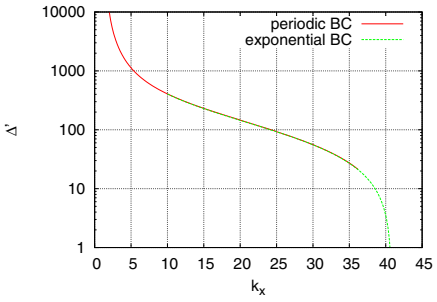

Fig. 10 (online colour at: www.an-journal.org) Δ' obtained with two boundary conditions.

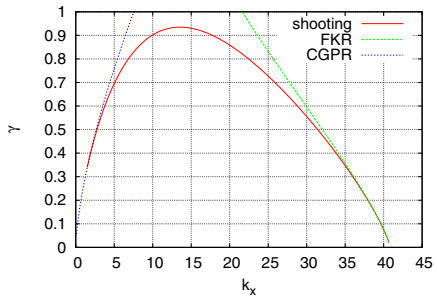

Fig. 11 (online colour at: www.an-journal.org) Dispersion relation of the slab tearing instability for the background profile of Fig. 6.

gent condition would be that the highest growth rate must be larger than v_r/L_r since otherwise the mode may be transferred away before it grows. We may estimate L_r by picking a specific value of the flux ψ and see how long it is elongated radially. Thus we need to obtain the growth rate.

The growth rate is shown with respect to k_x in Fig. 11 with a comparison to FKR and CGPR's analytic results. Our scheme fails for $k_x \lesssim 1.5$ since $b_z(z_{\rm sheet})$ becomes too close to zero and it erroneously changes sign. Nevertheless, the growth rate approaches the $\Delta' \to \infty$ limit, so that we may use analytic estimate for this region. In any case this does not cause any problem since the largest growth rate is captured by our numerical estimate.

The radial length of the stretched field line L_r may be evaluated by the radius at which the background ψ equals a particular value along $z = 0.75$ and $z = 0.25$ chosen well in the stretched field area. Taking $\psi = 0.025$ gives us $L_r(\psi = 0.025) \simeq 0.53$ and, as seen in Fig. 6, $v_r(z = 0.75) \simeq 0.062$. Thus

$$\gamma \frac{L_r}{v_r} \simeq 7.78 \gg 1, \tag{30}$$

which shows that the tearing mode grows fast enough before it is transferred away by the radial flow. It is noted that we don't have to worry about v_θ since the evolution is axisymmetric as far as this analysis is concerned.

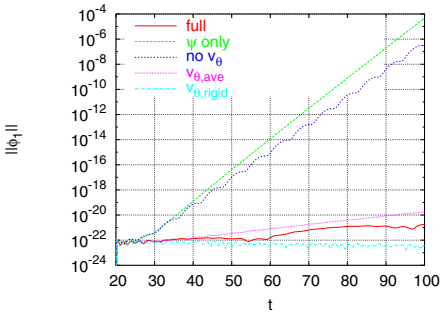

Fig. 12 (online colour at: www.an-journal.org) Time evolution of $||\phi_1||$ with various background setup. The lines labeled 'full' used full set of the background fields; 'ψ-only' retained only ψ_0 and set $\phi_0, v_{\theta,0}, B_{\theta,0} = 0$; 'no v_θ' retained ψ_0, ϕ_0 and $B_{\theta,0}$ with $v_{\theta,0} = 0$; '$v_{\theta,\rm ave}$' retained ψ_0, ϕ_0 and $B_{\theta,0}$ with only $v_{\theta,0}$ averaged along z; and '$v_{\theta,\rm rigid}$' retained ψ_0, ϕ_0 and $B_{\theta,0}$ with only $v_{\theta,0}$ replaced by a rigid rotation corresponding to the angular velocity $\Omega = 0.7$.

4.2 Linearized cylindrical simulation with a fixed background

Here we fix all field quantities at a given time in the full nonlinear simulation and evolve the linearized equation to see if there is any instability. We divide the quantities as $f = f_0 + f_1$, take the field of the nonlinear simulation at some instant as f_0, and fix it. Then we solve the linearized reduced MHD equations (same 2D cylindrical ones):

$$\partial_t \omega_1 + \left[\phi_0, \frac{\omega_1}{r}\right] + \left[\phi_1, \frac{\omega_0}{r}\right] + \frac{2}{r}\partial_z(v_{\theta,0} v_{\theta,1}) = \left[\psi_0, \frac{j_1}{r}\right] + \left[\psi_1, \frac{j_0}{r}\right] + \frac{2}{r}\partial_z(B_{\theta,0} B_{\theta,1}) + \nu \nabla_*^2 (r\omega_1), \tag{31}$$

$$\partial_t v_{\theta,1} + \frac{1}{r^2}\left([\phi_0, r v_{\theta,1}] + [\phi_1, r v_{\theta,0}]\right) = \frac{1}{r^2}\left([\psi_0, r B_{\theta,1}] + [\psi_1, r B_{\theta,0}]\right) + \nu \nabla_*^2 (r v_{\theta,1}), \tag{32}$$

$$\partial_t \psi_1 + \frac{1}{r}([\phi_0, \psi_1] + [\phi_1, \psi_0]) = \eta r j_1, \tag{33}$$

$$\partial_t B_{\theta,1} + \left[\phi_0, \frac{B_{\theta,1}}{r}\right] + \left[\phi_1, \frac{B_{\theta,0}}{r}\right] = \left[\psi_0, \frac{v_{\theta,1}}{r}\right] + \left[\psi_1, \frac{v_{\theta,0}}{r}\right] + \eta \nabla_*^2 (r B_{\theta,1}), \tag{34}$$

with a tiny initial perturbation on ω_1. The background field quantities (denoted with subscript zero) do not satisfy the equilibrium equations exactly, however, we may neglect the effect of their little imbalance as far as their changes are slow compared to the reconnection dynamics. As a validation test of the linearized version of the code, we have reproduced the growth rates and eigenfunctions of the primary MRI and tearing instability with $\tanh(r)$-like field profile.

The time evolution of the perturbed quantities are shown in Fig. 12 with the fixed background corresponding to $t = 20$ of the nonlinear simulation. Here we note that $t = 20$ corresponds to the time right before the appearance of the X-point (see Sect. 3). The lines labeled 'full' used full set

of the background fields; 'ψ-only' retained only ψ_0 and set ϕ_0, $v_{\theta,0}$, $B_{\theta,0} = 0$; 'no v_θ' retained ψ_0, ϕ_0 and $B_{\theta,0}$ with $v_{\theta,0} = 0$; '$v_{\theta,\mathrm{ave}}$' retained ψ_0, ϕ_0 and $B_{\theta,0}$ with only $v_{\theta,0}$ averaged along z; and '$v_{\theta,\mathrm{rigid}}$' retained ψ_0, ϕ_0 and $B_{\theta,0}$ with only $v_{\theta,0}$ replaced by a rigid rotation.

4.2.1 Stabilizing effect of rigid rotation

As ψ-only line shows, the flux function ψ_0 is tearing unstable with a comparable growth rate to the time scale of the reconnection ($\gamma \simeq 0.58$). The result with full background shows a very slow growth, while killing only v_θ immediately recovers the comparable growth rate to the ψ-only case. This fact suggests that $v_{\theta,0}$ has a strong stabilizing influence and the slab analysis we made in the previous section may be a too much simplification.

In order to confirm the stabilizing effect of $v_{\theta,0}$, we have turned on only the $k_z = 0$ component of the background v_θ (labeled $v_{\theta,\mathrm{ave}}$). The difference between no-v_θ and $v_{\theta,\mathrm{ave}}$ is only the average ($k_z = 0$) component of the background v_θ. From the significant decrease of the growth rate with the average v_θ component, we may conclude that the stabilizing effect is not given by the z-shear of v_θ, which in fact has a much larger length scale than the field reversal.

By the inspection of the radial profile of the angular velocity Ω (see Fig. 5), the radial Ω shear is highly localized around the inner wall for the averaged v_θ model we used in the linearized simulation. Thus we may conjecture that the stabilization may not be attributed to the radial Ω shear either. Instead the stabilizing effect may be caused by the centrifugal force.

In order to check our conjecture, we prepared a rigid v_θ profile

$$v_\theta(r) = 0.7r, \tag{35}$$

which gives rise to the constant angular velocity $\Omega = 0.7$, taken from the averaged angular velocity around the reconnection site. The result is shown in Fig. 12 with a label $v_{\theta,\mathrm{rigid}}$. From the fact that there is no growth at all for this case, we may draw the following conclusion. The tearing instability is completely stabilized due to the centrifugal force of the background rotation $v_{\theta,\mathrm{rigid}}$, and the slow growth shown in the full and $v_{\theta,\mathrm{ave}}$ simulations is a remnant of the magnetorotational instability, which is also indicated by the structure of the eigenfunction (not shown here).

It is interesting to find that centrifugal force seems to have a stabilizing effect while the similar conclusion is drawn for the gravitational field in the normal field case (Nishikawa & Sakai 1982; Paris 1987). The question is if the reconnection is completely forced. To answer this, we have to confirm the stabilization of tearing instability at every instant, which may be carried out by changing the time where background field is fixed.

Table 1 shows a summary of the linearized runs using the various choice of the retained background fields at several t. Finite growth rates labeled by $*$ have the eigenfunction structure corresponding to MRI. As seen in Table 1 we have tearing instability for ψ-only case, but not with rigid rotation until $t = 20$ (cases 1 and 6c). It is noted that for $t = 16$ we did not observe tearing instability even with ψ-only case. Comparison of cases 1, 2c and 4b for $t = 20$ and $t = 18$ tells us that the application of only rigid rotation do not completely stabilize the tearing instability, but that combined with B_θ does.

Table 1 Growth rates for various combination of the background field. In the field column, '$\circ$' denotes corresponding field is taken from the nonlinear simulation, while '–' denotes it is zeroed out. The labels 'ave' and 'rig' for v_θ denote the usage of average v_θ and rigid rotation. In the growth rate columns, '–' denotes no instability observed, and the numbers carrying '*' have MRI eigenfunctions.

Case	ψ	B_θ	ϕ	v_θ	$\gamma(t=21)$	$\gamma(t=20)$	$\gamma(t=18)$
1	$\circ$	–	–	–	0.47	0.58	0.64
2a	$\circ$	–	–	$\circ$		0.32	
2b	$\circ$	–	–	ave		0.40	
2c	$\circ$	–	–	rig	0.31	0.40	0.35
3	$\circ$	$\circ$	–	–	0.47	0.56	0.52
4a	$\circ$	$\circ$	–	$\circ$		–	0.33^*
4b	$\circ$	$\circ$	–	rig	0.23	–	–
5	$\circ$	$\circ$	$\circ$	–	0.37	0.50	0.13
6a	$\circ$	$\circ$	$\circ$	$\circ$	0.2	0.06^*	0.39^*
6b	$\circ$	$\circ$	$\circ$	ave		0.08^*	
6c	$\circ$	$\circ$	$\circ$	rig	0.17	–	–

4.2.2 Destabilization mechanism

At $t = 21$, however, we observed a tearing instability with a growth rate $\gamma \simeq 0.2$ for the full background field. The average angular velocity around reconnection site decreases only about 10%, but B_θ is only 50% of the $t = 20$ background. Since the effect of B_θ for finite v_θ is big (compare cases 2a/2c with 4a/4b), we may speculate that reduction of B_θ is affecting the destabilization. In fact by making the linearized simulation with $B_\theta(t = 20)$ and other fields at $t = 21$, the growth rate diminishes to $\gamma \simeq 0.03$. Thus the background field at $t = 20$ is almost marginal for tearing instability.

Figure 13 shows the eigenfunction of the 2D linearized simulation using the full background field of the nonlinear simulation at $t = 21$ sliced along $r \simeq 0.8$ and that of the 1D shooting calculation explained in the previous section using the 1D version of the same background. For the 1D shooting calculation we have taken $k_x = 20$ for which the growth rate achieves the maximum. The 2D eigenfunction structure suggests that $k_x \simeq 15$ along $z = 0.75$. It is shown that the eigenfunction structure becomes wider and Δ' seems smaller for the 2D calculation. The significant global change of the eigenfunction suggests that the effect of stabilizing mechanism due to centrifugal force and B_θ is global and we may need to reconstruct the theory including

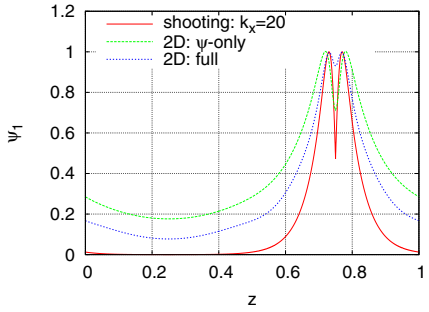

Fig. 13 (online colour at: www.an-journal.org) Eigenfunction taken from slab shooting analysis and 2D linearized simulation.

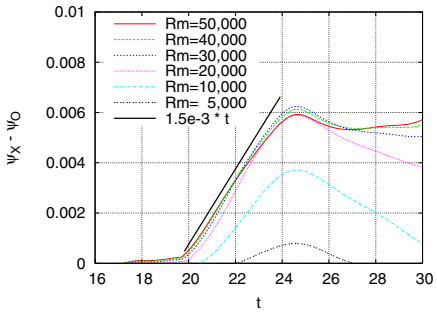

Fig. 14 (online colour at: www.an-journal.org) Time evolution of the reconnected flux $\psi_{\rm X} - \psi_{\rm O}$ at various $R_{\rm m}$.

Table 2 Critical magnetic Reynolds number for the appearance of the magnetic island in the nonlinear simulation and the corresponding tearing stability properties with 1D theory and 2D linearized simulation.

$R_{\rm m}$	1D tearing	γ of lin sim	2D NL sim
10 000	unstable	0.17	island
5 000	unstable	0.11	island
4 000	unstable	0.08	island
3 000	unstable	0.045	no island
2 000	unstable	—	no island
1 000	unstable	—	no island
750	stable	—	no island

the change of the outer solution. From the inspection of the 2D linear simulation result, the Δ' is estimated to be

$$\Delta' \simeq 12.0, \tag{36}$$

where we have used the largest gradient and the local minimum of ψ_1 around $z \simeq 0.75$ for its jump.

4.2.3 Critical magnetic Reynolds number

The effect of producing magnetic finger becomes weak as we decrease the Reynolds number due to the increase of the magnetic diffusivity. Thus the magnetic island ceases to appear for a sufficiently small magnetic Reynolds number. In such a case, we can compare the critical magnetic Reynolds number of the 2D nonlinear simulation, below which magnetic reconnection does not take place, with the linearized tearing instability calculation both for 1D theory and 2D simulation, and make it a validity test of our explanation.

The rough comparison is shown in Table 2. Here for the critical point of the 1D theory we used the coincidence of the quantity in the lhs of (30) to be unity. This condition may be too generous for the instability but it qualitatively shows an agreement with the appearance of the magnetic island in the nonlinear simulation. On the other hand the 2D linearized simulations show a much better agreement.

4.3 Reconnection rate

Figure 14 shows a plot of the reconnected flux $\psi_{\rm X} - \psi_{\rm O}$ versus time for various magnetic Reynolds numbers. Here we see two-step behaviors for $R_{\rm m} \gtrsim 20\,000$. This is because the background field is not unstable to tearing mode until $t \simeq 20$. The X-point is formed by the nonlinear effect of the overall evolution, however, the system is not tearing unstable yet. As soon as the background field enters tearing-unstable regime, the reconnection speeds-up, leading to the two-step behavior in the evolution of the island thickness and reconnected flux.

Figure 14 also shows that reconnection rate saturates around $R_{\rm m} \gtrsim 20,000$ and becomes independent of resistivity. From the linear fit, the reconnection rate is evaluated as

$$\frac{1}{v_{\rm Au}^2}\frac{{\rm d}(\psi_{\rm X} - \psi_{\rm O})}{{\rm d}t} \simeq 0.019, \tag{37}$$

where $v_{\rm Au}$ denotes the upstream Alfvén velocity for which we used a typical value of the maximum B_r along $r \simeq 0.8$ ($B_{r,\max} \simeq 0.28$).

There are other measures for the reconnection rate. The quantity $v_{\rm in}/v_{\rm Au}$ is one of them, which is

$$\max_{z\in(0.7,0.8)} \frac{v_{\rm in}}{v_{\rm Au}} \simeq 0.026 \tag{38}$$

at $r \simeq 0.82$ and $t = 21$ for the $R_{\rm m} = 10\,000$ run. The order-of-magnitude of this measurement is consistent with ${\rm d}(\psi_{\rm X} - \psi_{\rm O})/{\rm d}t$. This rate corresponds to slow reconnection as we expect from the usage of the resistive MHD model with a homogeneous resistivity.

Another measure may be given by $v_{\rm in}/v_{\rm out}$, which is

$$\frac{\max\limits_{z\in(0.7,0.8)} v_z(r \simeq 0.82)}{\max\limits_{r\in(0.6,1)} |v_r(z = 0.75)|} \simeq 0.22, \tag{39}$$

for the same situation. Note that $v_r(z = 0.75)$ is asymmetric with respect to the X-point and we may obtain the larger number when we use the maximum value within the island ($\simeq 0.38$). It is interesting to see $v_{\rm out}$ is so different from $v_{\rm Au}$, which normally have the same value in Sweet-Parker reconnection (Sweet 1958; Parker 1963). This is because of the finite size of the island. This fact is partly because the

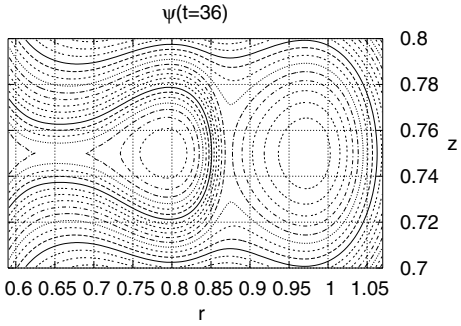

Fig. 15 Snapshot of the flux function at $t = 36$ for $R_{\rm m} = 30\,000$. Secondary magnetic island (inner one) appears for $R_{\rm m} \geq 2 \cdot 10^4$.

radial simulation box size is finite, but more crucial reason is the existence of the magnetic field at the outer region as well. In order to have a radially elongated island, the island has to push the outer magnetic field, which is resisted by the tension force of the field line. By only making a larger domain simulation doesn't help for enlarging $v_{\rm out}$.

5 Secondary reconnection

We find that the secondary island appears above $R_{\rm m} = 20\,000$ as shown in the contour plot of the flux function (Fig. 15). In these parameters, the aspect ratio of the current sheet exceeds 10 around $t \simeq 35$, which coincides with the simple theoretical argument of the threshold of tearing instability of the current sheet ($A > 2\pi$) (Biskamp 2000). Notice the difference of critical aspect ratio with the slab geometry (critical A seems much larger there, see Loureiro et al. 2005).

5.1 Linear analysis

In order to understand the secondary reconnection event we have made the linearized cylindrical simulation as in Sect. 4.2. Figure 16 shows the time evolution obtained from the linearized simulations for $R_{\rm m} = 20\,000$ with rigid rotation and full background field.

The time evolution of the perturbation amplitude shows a small difference in oscillation period but the growth rate is almost same. The place where the secondary reconnection takes place is around $r \simeq 0.7$ and $z \simeq 0.75$, so we show the slice along $r \simeq 0.7$ of the eigenfunction for the full background field case in Fig. 17. The flux function suggests a large Δ' and the instability is identified a strong tearing instability. As we've shown before, the aspect ratio of the current sheet for this case is $A \simeq 11.7$.

5.2 Bulanov's theory

Bulanov et al. (1979) points out that the expanding outflow along the current sheet has a stabilizing influence on the tearing instability, which is attributed to the much greater

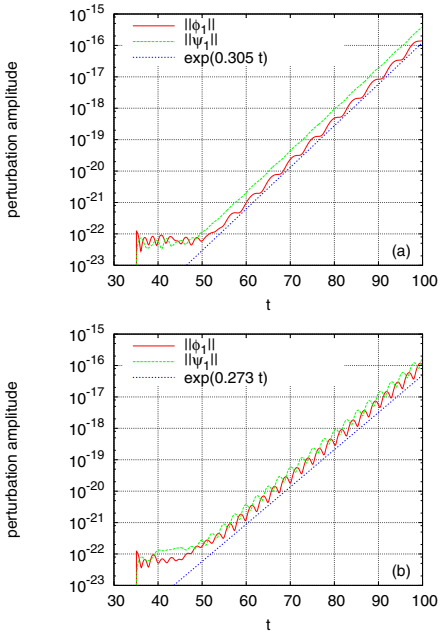

Fig. 16 (online colour at: www.an-journal.org) Growth of the perturbed field in the linearized 2D cylindrical simulation: (a) shows the results from rigid simulation with $\Omega = 0.7$ and (b) corresponds to the full background field at $t = 35$.

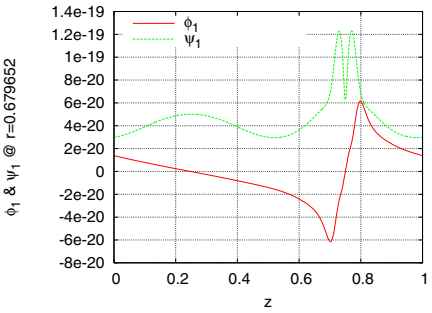

Fig. 17 (online colour at: www.an-journal.org) Slice of the eigenfunction for the secondary reconnection event.

critical aspect ratio in the slab geometry. The radial velocity profile in this case turns out

$$v_r(r \simeq r_X, z = 0.75) \simeq 1.5(r - r_X) + v_{r,X} \qquad (40)$$

at $t = 35$ and anti-symmetric around the X-point. According to the 2D cylindrical simulation of the linearized equations (same calculation with Sect. 4.2) without background ϕ, we obtained a growth rate of $\gamma \simeq 0.82$, which is more than double of that with the finite ϕ. Thus Bulanov's stabilizing effect is in fact effective in this case. It is also pointed out that Table 1 already shows a slight stabilizing tendency of ϕ on the tearing instability (Compare cases 3/4b and 5/6c). However, the v_r shear at this stage is very weak ($\mathrm{d}v_r/\mathrm{d}r \simeq 0.13$–$0.45$) compared to the present case.

Bulanov's analysis seems plausible qualitatively, however, the $\mathrm{d}v_r/\mathrm{d}r$ observed in (40) is almost twice as large as the growth rate without it. The stability condition $\mathrm{d}v_r/\mathrm{d}r \gtrsim$

γ_0 is satisfied but the configuration seems still unstable, where γ_0 is the growth rate without v_r. Thus the analysis given by Bulanov et al. is quantitatively unsatisfactory in our example.

6 Conclusion

We have numerically investigated the 2D magnetic reconnection during the nonlinear evolution of the MRI in the cylindrical geometry with rigid conducting walls. The outgoing radial jet is created in the inner region, which drags the initial axial field and forms a reversing radial field line configuration (magnetic finger). From the numerical simulations using our reduced MHD code, magnetic reconnection event is observed in the finger region (Sect. 3). However, unlike the theory by Goodman & Xu (1994) for the shearing slab geometry, the saturation is attributed to the radial flattening of the average angular velocity profile whose radial decrease has fed energy to the MRI (Sect. 3.2).

We have focused on the finger region and applied linear 1D and 2D theories (Furth et al. 1963; Coppi et al. 1976; Paris 1982; Nishikawa & Sakai 1982; Paris 1987). Slab 1D theory suggests that tearing instability can arise which may lead to the reconnection (Sect. 4.1), however, we need to invoke 2D analysis in order to explain the observation quantitatively (Sect. 4.2).

By the careful comparison to the conventional theories, we found that a new stabilizing effect must be present for explaining our results. The saturated MRI includes a radially flattened average angular velocity profile for a fairly wide regions. It corresponds to a rigid rotation whose centrifugal force has a stabilizing influence on the tearing instability. On the other hand, Kelvin-Helmholtz instability does not take place since the radial field strength is much stronger and is stabilized, although the radial outflow jet contains inflection points.

Therefore, the configuration is stable for a much higher field elongation even with a passively created X-point, and finally becomes tearing unstable and it is then when the reconnection speeds up (Sect. 4.3). It is interesting to point out that the creation of an X-point is not necessarily attributed to the tearing instability, but the reconnection is. The obtained reconnection rate has no dependence with respect to the resistivity for sufficiently high magnetic Reynolds number and corresponds to the slow reconnection rate as one might expect from the usage of the conventional MHD model.

In some parameter regimes we observe a creation of the secondary island which results from the tearing instability of the current sheet (Sect. 5). The threshold of the aspect ratio of the current sheet seems much smaller than the slab cases (Laureiro et al. 2005), and it is closer to the conventional argument of the tearing instability without any flow effects taken into account. However, the stabilizing effect of the flow is indeed observed, which suggests that the work by Bulanov et al. (1979) is qualitatively correct but not quantitatively. The stabilizing effect of the outflow is rather weak.

There are many things to be done to understand the dynamic properties of magnetic reconnection events. First, we need a theory about the centrifugal stabilization of the tearing instability. The effect of centrifugal (or gravitational) force perpendicular to the field reversal plane is analyzed in the early seminal paper (Furth et al. 1963), but that of the parallel one is unknown. According to the inspection of the eigenmode obtained numerically (Fig. 13), this effect is global and we need to modify the treatment of the outer region as well. To make such a theory may be rather involved, however, it should be important with various applications to the most astrophysical objects which include rotation and reconnection, such as accretion disks and earth's magnetotails. The secondary stability analysis from an exact stationary state may also be a good work in order to support our results here. In the real turbulent cases including fully turbulent MRI, we need to take the statistics of the reconnection events analysed here. From the viewpoint of the numerical simulation, it is very interesting to replace the physical model at the reconnection site with kinetic one and make a multiscale computation with a proper boundary condition, especially for the astrophysical applications.

For more close comparison with the observations of the laboratory experiments, it is highly desired to make a full three-dimensional (3D) analysis. In this case, things become more complicated. It may be especially interesting to ask whether tearing instability discussed here or 3D fluid instability (Davey et al. 1968) enters in the first place on the bifurcation diagram. In the non-magnetized fluid there is a transition to 3D mode as analyzed by Davey et al. (1968), however, such a disturbance seems easily stabilized by a superposition of an axial magnetic field (Tabeling 1981; Willis & Barenghi 2002). On the other hand, the magnetic reconnection may be easier for the 3D case than 2D since the MRI creates azimuthal magnetic field which contains reversing structure around the radial field reversal plane (See Fig. 6). Exploration of such a problem may be extremely helpful to understand the formation of nonaxisymmetric structures observed in the experiments (Sisan et al. 2004; Stefani et al. 2007).

Acknowledgements. Authors would like to thank Jim Drake, Richard Paris and François Rincon for valuable discussions.

References

Anderson, E., Bai, Z., Bischof, C., et al.: 1999, *LAPACK Users' Guide*, Soc. Ind. Appl. Math., Philadelphia
Balbus, S.A., Hawley, J.F.: 1991, ApJ 376, 214
Biskamp, D.: 1993, *Nonlinear Magnetohydrodynamics*, Cambridge Univ., Cambridge
Biskamp, D.: 2000, *Magnetic Reconnection in Plasmas*, Cambridge Univ., Cambridge
Bulanov, S.V., Sakai, J., Syrovatskii, S.I.: 1979, SvJPP 5, 157
Chandrasekhar, S.: 1960, Proc. Natl. Acad. Sci. USA 46, 253
Coppi, B., Galvao, R., Pellat, R., Rosenbluth, M.N.: 1976, SvJPP 2, 533
Coutsias, E.A., Hagstrom, T., Hesthaven, J.S., Torres, T.J.: 1996, Spec. Issue Houston J. Math., p. 21

Davey, A., Diprima, R.C., Stuart, J.T.: 1968, JFM 31, 17
Furth, H.P., Killeen, J., Rosenbluth, M.N.: 1963, PhFl 6, 459
Goodman, J., Xu, G.: 1994, ApJ 432, 213
Hawley, J.F., Balbus, S.A.: 1991, ApJ 376, 223
Hawley, J.F., Balbus, S.A.: 1992, ApJ 400, 595
Ji, H., Burin, M., Schartman, E., Goodman, J.: 2006, Nature 444, 343
Lazarian, A., Vishniac, E.T.: 1999, ApJ 517, 700
Liu, W., Goodman, J., Ji, H.: 2006, ApJ 643, 306
Loureiro, N.F., Cowley, S.C., Dorland, W., Haines, M.G., Schekochihin, A.A.: 2005, Phys Rev Lett 95, 235003
Machida, M., Matsumoto, R.: 2003, ApJ 585, 429
Nishikawa, K.-I., Sakai, J.: 1982, PhFl 25, 1384
Paris, R.B.: 1982, PlPh 24, 1541
Paris, R.B.: 1987, PhFl 30, 102
Parker, E.N.: 1963, ApJS 8, 177
Press, W.H., Flannery, B.P., Teukolsky, S.A., Vetterling, W.T.: 1988, *Numerical Recipes*, Cambridge Univ., Cambridge
Rincon, F., Ogilvie, G.I., Proctor, M.R.E.: 2007, Phys Rev Lett 98, 254502
Sisan, D.R., Mujica, N., Tillotson, W.A., Huang, Y.-M., Dorland, W., Hassam, A.B., Antonsen, T.M., Lathrop, D.P.: 2004, Phys Rev Lett 93, 114502
Stefani, F., Gundrum, T., Gerbeth, G., Rüdiger, G., Schultz, M., Szklarski, J., Hollerbach, R.: 2006, Phys Rev Lett 97, 184502
Stefani, F., Gundrum, T., Gerbeth, G., Rüdiger, G., Szklarski, J., Hollerbach, R.: 2007, NJPh 9, 295
Sweet, P.A.: 1958, NCimS 8, 188
Tabeling, P.: 1981, JFM 112, 329
Tanuma, S., Yokoyama, T., Kudoh, T., Shibata, K.: 2001, ApJ 551, 312
Tanuma, S., Yokoyama, T., Kudoh, T., Shibata, K.: 2003, ApJ 582, 215
Tatsuno, T., Dorland, W.: 2006, PhPl 13, 092107
Tillotson, W.A.: 2007, PhD Thesis
Velikhov, E.P.: 1959, SJETP 36, 995
Wang, Z., Si, J., Liu, W., Li, H.: 2007, preprint
Willis, A.P., Barenghi, C.F.: 2002, JFM 472, 399

A Numerical implementation

For our simulation we used a code developed by Tatsuno & Dorland (2006), however, we needed some upgrade in order to solve the cylindrical problem. In this section we describe the specific changes we have made for the cylindrical version. For notation refer Tatsuno & Dorland (2006) or Coutsias et al. (1996).

A.1 Preconditioning

Making the band matrix for the inversion becomes a little bit tricky because of the Jacobian and we end up with a denser matrix. Poisson equation

$$\nabla_*^2\phi = \omega \tag{A1}$$

is written as

$$\partial_r\left(\frac{1}{r}\partial_r\phi\right) + \frac{1}{r}\partial_z^2\phi = \partial_r^2\left(r\Phi\right) + \partial_r\Phi + \partial_z^2\left(r\Phi\right) = \omega, \tag{A2}$$

where $\Phi = \phi/r^2$. By multiplying ${}^{[2]}\mathcal{D}^{-2}$ on both sides from the left, ∂_r and ∂_r^2 are banded, and we obtain a band matrix on the left hand side:

$$\left[{}^{[2]}\mathcal{D}^{-2}\left(\partial_r^2 r + \partial_r - k_z^2 r\right)\right]\Phi = {}^{[2]}\mathcal{D}^{-2}\omega. \tag{A3}$$

By inverting it and multiplying r^2, we obtain ϕ. We used LAPACK for the inversion of these banded matrix (Anderson et al. 1999).

A.2 Time integration

The equations for ω, v_θ, and B_θ share their form

$$\partial_t f = \mathcal{NL} + \mu\nabla_*^2(rf), \tag{A4}$$

where f is one of the ω, v_θ, or B_θ, $\mathcal{NL}$ is a symbolic expression for the nonlinear term, and μ is the diffusion coefficient, ν or η. The diffusion term is treated implicitly, using Crank-Nicholson scheme. The time derivative and Laplacian terms are discretized as

$$\frac{f^{n+1}-f^n}{\Delta t} = \mathcal{NL} + \mu\nabla_*^2\left(r\,\frac{f^{n+1}+f^n}{2}\right), \tag{A5}$$

where the superscript denotes the time step. By manipulation and multiplication of ${}^{[2]}\mathcal{D}^{-2}$, we obtain a banded matrix on the left hand side:

$$\begin{aligned}&{}^{[2]}\mathcal{D}^{-2}\left[r - \mu\frac{\Delta t}{2}\left(\partial_r^2 r + \partial_r - k_z^2 r\right)\right]\frac{f^{n+1}}{r}\\ &= {}^{[2]}\mathcal{D}^{-2}\left[f^n + \Delta t\mathcal{NL} + \mu\frac{\Delta t}{2}\nabla_*^2(rf^n)\right].\end{aligned} \tag{A6}$$

The boundary conditions on f are converted to the ones on f/r, and implemented in the first two rows of (A6).

The equation for ψ has a different form:

$$\partial_t\psi = \mathcal{NL} + \eta r\nabla_*^2\psi \tag{A7}$$

thus its discretization yields

$$\frac{\psi^{n+1}-\psi^n}{\Delta t} = \mathcal{NL} + \eta r\nabla_*^2\left(\frac{\psi^{n+1}+\psi^n}{2}\right). \tag{A8}$$

Manipulation and multiplication of ${}^{[2]}\mathcal{D}^{-2}$ on both sides yields

$$\begin{aligned}&{}^{[2]}\mathcal{D}^{-2}\left[r^2 - \eta\frac{\Delta t}{2}\left(\partial_r^2 r^2 - \partial_r r - 1 - k_z^2 r^2\right)\right]\Psi^{n+1}\\ &\qquad = {}^{[2]}\mathcal{D}^{-2}\left(\psi^n + \Delta t\mathcal{NL} + \eta\frac{\Delta t}{2}rj\right),\end{aligned} \tag{A9}$$

where we used $\Psi = \psi/r^2$ and

$$r\nabla_*^2\psi = \partial_r^2(r^2\Psi) - \partial_r(r\Psi) - \Psi + r^2\partial_z^2\Psi. \tag{A10}$$

A.3 Two-step Sherman-Morrison formula

Tatsuno & Dorland (2006) succeeded to make a band matrix with single extra dense row by splitting the matrix equation into odd and even parts of the Chebyshev coefficients. However, since they are coupled in the cylindrical geometry, we have two dense rows related to the boundary conditions. We solve this problem by applying Sherman-Morrison formula twice (Press et al. 1988).

Let $\mathcal{A}$ be the perturbed matrix

$$\mathcal{A} = \underbrace{\mathcal{A}_0 + \boldsymbol{u}_1\otimes\boldsymbol{v}_1}_{\mathcal{A}_1} + \boldsymbol{u}_2\otimes\boldsymbol{v}_2, \tag{A11}$$

where $\mathcal{A}_0$ is the band matrix and $\boldsymbol{u}_{1,2}$ $\boldsymbol{v}_{1,2}$ are the vectors. We want to solve

$$\mathcal{A}\boldsymbol{x} = \boldsymbol{b}. \tag{A12}$$

Then, from Sherman-Morrison formula, the solution of

$$(\mathcal{A}_1 + \boldsymbol{u}_2 \otimes \boldsymbol{v}_2)\boldsymbol{x} = \boldsymbol{b} \tag{A13}$$

is obtained by solving

$$\mathcal{A}_1 \boldsymbol{y} = \boldsymbol{b} \qquad \mathcal{A}_1 \boldsymbol{z}_2 = \boldsymbol{u}_2 \tag{A14}$$

as

$$\boldsymbol{x} = \boldsymbol{y} - \frac{\boldsymbol{v}_2 \cdot \boldsymbol{y}}{1 + \boldsymbol{v}_2 \cdot \boldsymbol{z}_2}\boldsymbol{z}_2. \tag{A15}$$

The solution of

$$\mathcal{A}_1 \boldsymbol{y} = \boldsymbol{b} \tag{A16}$$

is obtained by solving

$$\mathcal{A}_0 \boldsymbol{x}_1 = \boldsymbol{b} \qquad \mathcal{A}_0 \boldsymbol{z}_1 = \boldsymbol{u}_1 \tag{A17}$$

as

$$\boldsymbol{y} = \boldsymbol{x}_1 - \frac{\boldsymbol{v}_1 \cdot \boldsymbol{x}_1}{1 + \boldsymbol{v}_1 \cdot \boldsymbol{z}_1}\boldsymbol{z}_1. \tag{A18}$$

The solution of

$$\mathcal{A}_1 \boldsymbol{z}_2 = \boldsymbol{u}_2 \tag{A19}$$

is obtained by solving

$$\mathcal{A}_0 \boldsymbol{z}_2' = \boldsymbol{u}_2 \qquad \mathcal{A}_0 \boldsymbol{z}_2'' = \boldsymbol{u}_1 \tag{A20}$$

as

$$\boldsymbol{z}_2 = \boldsymbol{z}_2' - \frac{\boldsymbol{v}_1 \cdot \boldsymbol{z}_2'}{1 + \boldsymbol{v}_1 \cdot \boldsymbol{z}_2''}\boldsymbol{z}_2'' \tag{A21}$$

where $\boldsymbol{z}_2''$ turns out to be $\boldsymbol{z}_2'' = \boldsymbol{z}_1$.

B Analytic estimate of 2D tearing

In this section we discuss the stabilizing effect of the gravitational force in the two-dimensional magnetic field configuration in order to point out the similarity to the centrifugal stabilization. This effect is pointed out by the numerical calculation in Nishikawa & Sakai (1982) and implicitly obtained by the analytic calculation of Paris (1987). In this section we briefly revisit the result of Paris and discuss the similarity to the centrifugal force. For the full detail of the analysis, refer to the original paper (Paris 1987).

B.1 Dispersion relation

When we add a normal in-plane field such as the case of earth's magnetotail, the equilibrium has to be sustained by the gravitational force in order to balance the tension force of the magnetic field. However, when the normal field is weak, to the leading order, the outer region equation can be described by the same second order ODE without the normal field (Furth et al. 1963).

The effects of the weak normal field and the gravitational force enter in the resistive layer equation and the proper analysis leads to the following dispersion relation:

$$\Delta' = \frac{2^{7/2}\pi\Omega}{1-(4\kappa)^2}\frac{\Gamma(3/4+\kappa)}{\Gamma(1/4+\kappa)}H, \tag{B1}$$

where

$$H = \frac{1 + 2\sigma\lambda_G}{\Lambda^{3/2}\left[1 - \dfrac{2\sigma\lambda\lambda_G}{\Lambda(1-4\kappa)}\left(1 - \dfrac{1-c/\Lambda}{3+4\kappa}\bar{F}(1)\right)\right]} \tag{B2}$$

$$\bar{F}(n) = {}_2F_1\left(\frac{1}{2}, n; \frac{7}{4}+\kappa; \frac{1-c/\Lambda}{2}\right). \tag{B3}$$

Here ${}_2F_1$ is a hypergeometric function, λ_G the effect of the gravitational force, σ the effect of the normal field, and

$$\Lambda = [1 + \lambda_G(2\sigma - \lambda_G)]^{1/2}, \tag{B4}$$

$$c = \mathrm{i}(\lambda_G - \sigma), \tag{B5}$$

$$\kappa = \frac{\lambda + \mathrm{i}\lambda_G}{4\Lambda}. \tag{B6}$$

We only give here a minimal set of description for our purpose. For the full description of the variables refer to the original paper (Paris 1987).

B.2 Implication of Paris' dispersion relation

Let us think about the artificial cases with

1. $\sigma \neq 0$ and $\lambda_G = 0$,
2. $\lambda_G \neq 0$ and $\sigma = 0$.

It is true that these assumptions break the equilibrium condition, but they are still helpful in understanding the effect of each term. In case 1, we obtain

$$\Lambda = 1, \quad c = -\mathrm{i}\sigma, \quad \kappa = \frac{1}{4}\lambda, \quad H = 1, \tag{B7}$$

which exactly recovers the dispersion relation after Eq.(14) of Paris. The effect of the normal field has completely diminished by only making $\lambda_G = 0$.

On the other hand, case 2 leaves out a finite effect of gravity since

$$\Lambda = \sqrt{1-\lambda_G^2} < 1, \qquad c = \mathrm{i}\lambda_G,$$
$$\kappa = \frac{\lambda + \mathrm{i}\lambda_G}{4\sqrt{1-\lambda_G^2}}, \qquad H = \Lambda^{-3/2} > 1. \tag{B8}$$

Defining the effective Δ' by

$$\Delta'_{\mathrm{eff}} = \frac{\Delta'_{\mathrm{orig}}}{H} < \Delta'_{\mathrm{orig}}, \tag{B9}$$

where Δ'_{orig} is the value matched with outer solutions, we see that for a finite λ_G, (i) the effective Δ' becomes smaller, and (ii) λ becomes smaller for a given κ (due to the smaller denominator), both of which suggest stabilizing influence. It is noted, however, that the second statement may not exactly apply because the imaginary number $\mathrm{i}\lambda_G$ is also added in the numerator.

